



# Calcium isotopic ratios and rare earth element abundances in refractory inclusions from the Allende CV3 chondrite

Shichun Huang<sup>\*</sup>, Juraj Farkaš<sup>1,2</sup>, Gang Yu, Michail I. Petaev<sup>3</sup>, Stein B. Jacobsen

*Department of Earth and Planetary Sciences, Harvard University, 20 Oxford Street, MA 02138, United States*

Received 14 April 2011; accepted in revised form 1 November 2011

## Abstract

Refractory inclusions in primitive meteorites are the oldest objects formed in the Solar System. They exhibit large mass-dependent isotopic effects in many elements, including Si, Mg and Ca, indicative of their complex origin. We report data for both mass-dependent ( $\delta$ ) and mass-independent ( $\epsilon$ ) Ca isotopic effects, and rare earth element (REE) abundances in six refractory inclusions from the Allende CV3 meteorite. Our data reveal large mass-dependent Ca isotopic effects in these refractory inclusions, with  $\delta^{44/40}\text{Ca}$  ranging from  $-5.60$  to  $+0.35$  (relative to NIST SRM 915a), which are significantly lower than that of the bulk silicate Earth ( $\delta^{44/40}\text{Ca} = 1.05 \pm 0.04$ ). Importantly,  $\delta^{44/40}\text{Ca}$  is correlated with REE patterns: refractory inclusions with Group II REE patterns have lighter Ca isotope compositions compared to those with Group I REE patterns. Specifically, the studied refractory inclusions form negative  $^{44}\text{Ca}/^{40}\text{Ca}$ –Tm/Er and  $^{44}\text{Ca}/^{40}\text{Ca}$ –Nd/Er trends, implying segregation of up to 3% of an ultrarefractory evaporation residue from a chondritic reservoir prior to the formation of refractory inclusions. This residue would have to be characterized by high  $^{44}\text{Ca}/^{40}\text{Ca}$  and low Tm/Er and Nd/Er. At  $2\sigma$  levels of  $\pm 0.5$  and  $\pm 1.5$  for  $\epsilon^{40/44}\text{Ca}$  and  $\epsilon^{43/44}\text{Ca}$ , respectively, the six refractory inclusions studied show no detectable  $^{40}\text{Ca}$  or  $^{43}\text{Ca}$  anomalies relative to the terrestrial standards. However, five out of the six refractory inclusions do show a  $^{48}\text{Ca}$  excess of several  $\epsilon$ -units, clearly resolvable from the terrestrial standards.

© 2011 Elsevier Ltd. All rights reserved.

## 1. INTRODUCTION

Refractory inclusions – the calcium–aluminum-rich inclusions (CAIs) and amoeboid olivine aggregates (AOAs) – are the first condensates from the solar nebula (Grossman and Larimer, 1974), and represent the oldest objects formed in the Solar System (Gray et al., 1973; Amelin et al., 2002,

2010). The origin of refractory inclusions is related to high-temperature condensation/evaporation processes in the solar nebula (e.g., MacPherson et al., 1988; Ireland and Fegley, 2000; Richter et al., 2002; MacPherson, 2004). Many refractory inclusions have igneous textures, with some having been modified by secondary alteration processes (e.g., MacPherson, 2004). Refractory inclusions exhibit both large mass-dependent and mass-independent isotopic effects in many elements (Clayton et al., 1973; McCulloch and Wasserburg, 1978a,b; Lee et al., 1979, 2011; Jungck et al., 1984; Niederer and Papanastassiou, 1984; Papanastassiou, 1986; Birck and Lugmair, 1988; Harper, 1993; Yin et al., 2002; Grossman et al., 2008; Krot et al., 2008; MacPherson et al., 2008; Bermingham and Mezger, 2010). Some mass-independent isotopic effects in refractory inclusions, such as  $^{48}\text{Ca}$ ,  $^{50}\text{Ti}$ ,  $^{54}\text{Cr}$ ,  $^{95}\text{Mo}$ ,  $^{100}\text{Mo}$ ,  $^{135}\text{Ba}$ ,  $^{137}\text{Ba}$  and  $^{144}\text{Sm}$  (McCulloch and Wasserburg, 1978a,b; Jungck et al., 1984; Niederer and Papanastassiou, 1984; Papanastassiou,

<sup>\*</sup> Corresponding author.

E-mail addresses: [huang17@fas.harvard.edu](mailto:huang17@fas.harvard.edu) (S. Huang), [jacobsen@neodymium.harvard.edu](mailto:jacobsen@neodymium.harvard.edu) (S.B. Jacobsen).

<sup>1</sup> Present address: Faculty of Environmental Sciences, Czech University of Life Sciences, Kamýčka 129, Prague 6, Suchbát 165 21, Czech Republic.

<sup>2</sup> Also at Department of Geochemistry, Czech Geological Survey, Geologická 6, 152 00, Prague 5, Czech Republic.

<sup>3</sup> Also at Harvard-Smithsonian Center for Astrophysics, 60 Garden Street, Cambridge, MA 02138, United States.

1986; Yin et al., 2002), reflect incomplete mixing of isotopically anomalous pre-solar grains. Many refractory inclusions show  $^{26}\text{Mg}$  excess (due to  $^{26}\text{Al}$  decay, Lee et al., 1977; Jacobsen et al., 2008a,b) and some show  $^{41}\text{K}$  excess (due to  $^{41}\text{Ca}$  decay, Srinivasan et al., 1996). The presence of short-lived nuclei indicates that many refractory inclusions formed during the very early Solar System in a short time interval, most likely less than 100,000 yr (Connelly et al., 2008). The very large mass-dependent isotopic fractionations in Mg, Si, Ca and O isotopes point to important roles of condensation and evaporation in the formation and evolution of refractory inclusions. Among the refractory inclusions studied for Mg, Si and Ca isotopes, many exhibit correlated enrichments in heavy Mg and Si isotopes relative to the composition of the bulk silicate Earth, but they generally have lighter Ca isotopes that are not correlated with Mg or Si isotopic effects (Niederer and Papanastassiou, 1984; Clayton et al., 1988). Hence, the observed heavier Mg and Si isotopes and lighter Ca isotopes in refractory inclusions cannot be explained by a single-stage evaporation or condensation process. Rather this implies that the fractionation of Mg, Si and Ca isotopes occurred at different stages of refractory inclusion evolution (Niederer and Papanastassiou, 1984).

Rare earth elements (REEs) are also fractionated from each other during evaporation or condensation process according to their volatilities (e.g., Boynton, 1975; Davis and Grossman, 1979). Several types of REE patterns have been observed in refractory inclusions (e.g., Tanaka and Masuda, 1973; Mason and Martin, 1977; Mason and Taylor, 1982; Boynton, 1984; MacPherson et al., 1988; Ireland and Fegley, 2000; MacPherson, 2004). Five distinct REE patterns have been classified by Mason and Martin (1977). Groups I, III, V and VI REE patterns are essentially flat at  $\sim 20\times$  enrichment relative to the CI chondrites, with relative enrichments or depletions in the most volatile REEs (Eu and Yb). The Group II REE pattern, first identified by Tanaka and Masuda (1973), is depleted in the most refractory REEs (heavy REEs except for Tm and Yb), and it is characterized by a positive Tm anomaly. An ultrarefractory REE pattern is characterized by the enrichment in the super-refractory REEs, and is roughly complementary to the Group II REE pattern. This type of REE pattern has been identified in platy hibonite crystals and CAIs (MH-115, HIB-11) from CM2 Murchison (Boynton et al., 1980; Ireland et al., 1988; Simon et al., 1996, 2002), in a CAI from CV3 Efremovka (El Goresy et al., 2002), and in an ultrarefractory nodule from the CV3 Allende (Hiyagon et al., 2003).

Because REEs tend to partition into Ca-bearing minerals, such as melilite, perovskite and hibonite (e.g., Beckett et al., 2006), and volatility fractionation of REEs and Ca isotopic fractionation occur at the same temperature range (e.g., MacPherson and Davis, 1994), one would expect a correlation between Ca isotopic fractionation and REE patterns (e.g., Niederer and Papanastassiou, 1984). In order to test this idea, we measured both the REE abundances and Ca isotopic compositions in six refractory inclusions from the Allende CV3 chondrite.

## 2. SAMPLES

Aliquots of six refractory inclusions from the Allende CV3 chondrite were chosen for this study. Three inclusions – GFG, WFG, and CGI – have been previously studied using SEM technique and analyzed for Sm and Nd isotopes at Johannes Gutenberg Universität in Mainz (Bogdanovski, 1997), and powders of these refractory inclusions, left after the Sm–Nd isotopic work, were used in this study. Three others inclusions – SJ101, SJ102, and SJ103 – were extracted from the Allende meteorite at Harvard University. They were studied using petrographic and EPMA techniques, and analyzed for Mg isotopes (Jacobsen et al., 2008b; Petaev and Jacobsen, 2009). These refractory inclusions form a positive  $^{27}\text{Al}/^{24}\text{Mg}$ – $^{26}\text{Mg}$  trend, with a canonical  $^{26}\text{Al}/^{27}\text{Al}$  value of  $5.25 \times 10^{-5}$  (Jacobsen et al., 2008b).

The GFG (gray fined-grained) inclusion,  $\sim 9 \times 4$  mm in size, consists mainly of FeO-rich olivine ( $\text{Fo}_{93}$ – $\text{Fo}_{82}$ ), FeO-poor and FeO-rich clinopyroxenes, subordinate amounts of nepheline and sodalite, and rare small grains of magnesian spinel ( $X_{\text{Mg}} = 0.71 - 0.76$ ) (Bogdanovski, 1997). The mineral chemistry of GFG points to a severe secondary alteration due to the interaction with a Fe, Na and Cl-rich fluid on the Allende parent body.

The WFG (white fine-grained) inclusion,  $\sim 8 \times 3$  mm in size, was identified as a spinel-rich fine-grained CAI. It consists mainly of numerous anhedral spinel grains with clinopyroxene, perovskite, feldspathoids, and garnets interspersed among them. The inclusion has experienced substantial secondary alteration as suggested by the significant FeO contents in spinel, perovskite, and pyroxene (Bogdanovski, 1997).

The compact CGI (coarse-grained) CAI,  $\sim 11 \times 5$  mm in size, consists of a large core of coarse-grained spinel, anorthite, and Al–Ti-rich clinopyroxene surrounded by a narrow (0.7–2 mm) mantle of fine-grained FeO-rich olivine. The mineralogy, as well as the ‘lacy’ texture of the anorthite-clinopyroxene intergrowths, are characteristic of Type C CAIs. The rather high FeO contents in olivine and clinopyroxene as well as abundant nepheline are indicative of substantial secondary alteration (Bogdanovski, 1997).

SJ101 is a large (6.34 g,  $\sim 25 \times 15$  mm), forsterite-bearing Type B CAI described in detail by Petaev and Jacobsen (2009). It consists of large coarse-grained grossular-melilite-anorthite-clinopyroxene domains separated by sinuous finer-grained forsterite-clinopyroxene bands. The numerous small spinel grains enclosed in silicates are distributed homogeneously throughout the inclusion. Although minor amounts of andradite and nepheline are present in the cavities and on the periphery of SJ101, the low FeO contents in silicates and spinel suggest that the bulk of SJ101 has escaped secondary alteration.

SJ102 is a small ( $\sim 5$  mm) spherical Type B1 CAI. It consists of coarse-grained  $\text{TiO}_2$ -rich clinopyroxene and  $\text{Al}_2\text{O}_3$ -rich melilite which poikilitically enclose abundant euhedral grains or clusters of nearly pure spinel ( $\text{MgAl}_2\text{O}_4$ ). The mantle melilite is zoned, with the MgO content decreasing outward from  $\sim 8$  wt.% near the boundary with clinopyroxene down to  $\sim 2$  wt.% at the periphery of the inclusion. Melilite displays irregular patches of alteration products,

which mainly consist of grossular and, to a lesser, extent anorthite. Remnants of the Wark-Lovering rim are represented by thin discontinuous bands of FeO-rich spinel at the interface with the matrix. The FeO- and/or Na<sub>2</sub>O-rich patches of secondary alteration are mainly observed at the periphery of the inclusion and along cracks in melilite.

SJ103 is a small (~10 mm) irregular Type B2 CAI. It consists of low-TiO<sub>2</sub> clinopyroxene, anorthite, Al<sub>2</sub>O<sub>3</sub>-rich melilite, and nearly pure spinel. The melilite and clinopyroxene show only minor zoning. The “classic” Wark-Lovering rim contains large anhedral masses of spinel and perovskite along with small blades of Mg-bearing hibonite. The Fe and Na X-ray maps show minor secondary alteration, with Fe and Na apparently being decoupled. The FeO-bearing clinopyroxene and spinel are restricted to the external 100–150 μm of the inclusion, mainly to the Wark-Lovering rim. The Na-bearing, very fine-grained assemblage typically occurs as branching, narrow (<20 μm) bands along grain boundaries or cracks in melilite throughout the inclusion.

### 3. ANALYTICAL DETAILS

Small rock chips of refractory inclusions SJ101, SJ102 and SJ103, and powdered refractory inclusions WFG, GFG and CGI, ranging from several to several tens of mg, were dissolved in a 1:1 mixture of concentrated HF and HNO<sub>3</sub> acids using 6 ml standard square body Teflon vials at 120 °C for 2 weeks. After the HNO<sub>3</sub>–HF step, the sample solutions were dried down. Then they were dissolved using 1 ml concentrated HNO<sub>3</sub>. The sample solutions were then dried down three times with concentrated HNO<sub>3</sub> and once with 6 N HCl in order to break down insoluble CaF<sub>2</sub>. Finally, the samples were dissolved with an appropriate amount of 2.5 N HCl to form a 10 μg Ca/μL solution. No residue was observed in any of our samples. This digestion procedure was proven not to introduce any Ca isotopic fractionation (Huang et al., 2010). Three

separate aliquots were taken from each sample solution for REE elemental and Ca isotopic measurements.

#### 3.1. REE abundance analysis

Aliquots of sample solutions were diluted with 1.5% HNO<sub>3</sub> to make 1:5000 solutions, which were then analyzed for REE abundances by traditional solution-ICP-MS technique using a GV Platform XS Quadrupole ICP-MS at Harvard University. The monitored REE isotopes are: <sup>139</sup>La, <sup>140</sup>Ce, <sup>141</sup>Pr, <sup>143</sup>Nd, <sup>145</sup>Nd, <sup>147</sup>Sm, <sup>149</sup>Sm, <sup>152</sup>Sm, <sup>151</sup>Eu, <sup>153</sup>Eu, <sup>157</sup>Gd, <sup>158</sup>Gd, <sup>160</sup>Gd, <sup>159</sup>Tb, <sup>163</sup>Dy, <sup>165</sup>Ho, <sup>167</sup>Er, <sup>169</sup>Tm, <sup>172</sup>Yb, <sup>174</sup>Yb and <sup>175</sup>Lu. USGS standard samples, AGV-1, BCR-1 and BHVO-1, whose trace element abundances were given in Table A2 of Huang and Frey (2003), were used to construct the standard calibration curve. Each analytical sequence contained three standard sample solutions (BHVO-1, BCR-1 and AGV-1), one procedure blank, four unknown sample solutions, and one BHVO-2 or BHVO-1 solution analyzed as unknown sample. A BHVO-1 solution was analyzed every fifth solution in order to monitor the sensitivity drift. Each analytical sequence took about one hour. The sensitivity drifts for all analyzed isotopes were less than 20%, and most were less than 10%. Therefore, no internal drift monitor was used at Harvard during this study. Analytical uncertainties for all REEs are better than 5%, which were estimated using multiple measurements of BHVO-2 and BHVO-1 solutions treated as unknown samples. REE abundances of these six refractory inclusions are given in Table 1.

#### 3.2. Ca isotopic measurements

##### 3.2.1. Three origins of Ca isotopic effects

There are three processes known to cause Ca isotopic effects in refractory inclusions: 1. isotopic fractionation; 2. radiogenic <sup>40</sup>Ca excess due to <sup>40</sup>K decay; and 3. addition of nucleosynthetic components with non-solar isotopic compositions. In order to decipher these three types of Ca

Table 1a

Mass-dependent and mass-independent (mass-fractionation corrected) Ca isotopic effects in six refractory inclusions.

	GROUP I		N-GROUP II		A-GROUP II		SRM 915a	Seawater	San Carlos	Kilbourne Hole	BCR-1
	SJ103	CGI	SJ101	WFG	SJ102	GFG			Clinopyroxene	Clinopyroxene	
Mass-dependent Ca isotopic effects											
$\delta^{44/40}\text{Ca}$	−1.13	0.35	−3.80	−1.71	−3.45	−5.60	0.04	1.90			
$2\sigma_m$	0.06	0.02	0.12	0.03	0.08	0.05	0.02	0.03			
$\delta^{42/40}\text{Ca}$	−0.58	0.22	−1.98	−0.93	−1.76	−2.83	0.00	1.00			
$2\sigma_m$	0.03	0.03	0.04	0.05	0.13	0.05	0.04	0.06			
$\delta^{44/42}\text{Ca}$	−0.55	0.13	−1.82	−0.78	−1.68	−2.77	0.05	0.88			
$2\sigma_m$	0.06	0.04	0.09	0.01	0.15	0.02	0.03	0.03			
Mass-independent Ca isotopic effects											
$\varepsilon^{40/44}\text{Ca}$	0.8	−0.1	0.0	0.4	0.7	−0.9	0.00	−0.41	−0.3	−0.5	0.1
$2\sigma_m$	0.6	0.3	0.5	0.8	1.1	0.5	0.44	0.50	0.5	1.1	0.6
$\varepsilon^{43/44}\text{Ca}$	0.8	0.3	−0.5	1.2	0.9	0.7	0.00	−0.04	1.6	−0.7	0.3
$2\sigma_m$	1.8	1.1	1.6	1.4	1.1	1.4	0.73	1.34	1.4	1.9	1.2
$\varepsilon^{48/44}\text{Ca}$	3.2	8.2	2.5	5.2	−1.1	4.2	0.00	0.87	0.3	−0.9	0.7
$2\sigma_m$	1.7	4.4	1.7	1.8	1.7	1.6	0.66	1.21	0.8	1.4	0.9

We note that, as a tradition, the reported  $\delta^{44/40}\text{Ca}$  in many publications are followed by a “‰” symbol. However, this per mil symbol is redundant following the  $\delta$  notation definition, and it is very misleading to readers who are not familiar with stable isotopic research.

Table 1b

Rare earth element abundances (in ppm) in six refractory inclusions.

	GROUP I		N-GROUP II		A-GROUP II		BHVO-1	BHVO-2
	SJ103	CGI	SJ101	WFG	SJ102	GFG		
La	4.59	5.15	4.33	3.47	1.01	26.25	15.9	15.1
Ce	12.7	13.5	12.2	8.7	3.08	52.6	38.8	36.6
Pr	1.85	2.16	1.83	1.42	0.43	10.0	5.33	5.32
Nd	9.01	11.0	9.25	7.27	2.00	53.0	24.74	23.95
Sm	3.15	3.68	2.92	2.46	0.74	14.1	6.18	6.06
Eu	1.03	1.56	0.59	0.39	0.56	0.28	2.05	1.98
Gd	3.56	4.56	1.87	1.50	0.19	9.90	5.98	5.71
Tb	0.72	1.01	0.31	0.29	0.023	1.95	0.93	0.91
Dy	5.02	6.83	1.66	1.29	0.15	9.29	5.29	5.20
Ho	1.10	1.73	0.14	0.14	0.044	0.81	0.97	0.98
Er	3.29	5.50	0.34	0.36	0.11	1.57	2.51	2.48
Tm	0.57	0.71	0.53	0.46	0.10	2.05	0.36	0.35
Yb	3.27	4.45	1.60	1.22	0.64	0.60	2.04	2.00
Lu	0.52	1.04	0.038	0.033	b.d.	0.14	0.28	0.28

b.d.: below detection limit.

isotopic effects in the studied refractory inclusions, we report data for both mass-dependent and mass-independent Ca isotopic effects. The mass-dependent Ca isotopic effects are reported using the  $\delta$  notation ( $\delta^{44/40}\text{Ca}$ ,  $\delta^{42/40}\text{Ca}$  and  $\delta^{44/42}\text{Ca}$ ) relative to NIST SRM 915a (Eqs. (1)–(3)) as a measure of the natural isotopic variations intrinsic to the samples. In our study the instrumental isotopic fractionation is corrected by applying a  $^{43}\text{Ca}$ – $^{48}\text{Ca}$  double spike technique to obtain the *true*  $^{44}\text{Ca}/^{40}\text{Ca}$  (relative to NIST SRM 915a) in the sample:

$$\delta^{44/40}\text{Ca} = \left[ \frac{\left( \frac{^{44}\text{Ca}}{^{40}\text{Ca}} \right)_{\text{sample}}}{\left( \frac{^{44}\text{Ca}}{^{40}\text{Ca}} \right)_{\text{SRM 915a}}} - 1 \right] \times 10^3 \quad (1)$$

$$\delta^{42/40}\text{Ca} = \left[ \frac{\left( \frac{^{42}\text{Ca}}{^{40}\text{Ca}} \right)_{\text{sample}}}{\left( \frac{^{42}\text{Ca}}{^{40}\text{Ca}} \right)_{\text{SRM 915a}}} - 1 \right] \times 10^3 \quad (2)$$

$$\delta^{44/42}\text{Ca} = \left[ \frac{\left( \frac{^{44}\text{Ca}}{^{42}\text{Ca}} \right)_{\text{sample}}}{\left( \frac{^{44}\text{Ca}}{^{42}\text{Ca}} \right)_{\text{SRM 915a}}} - 1 \right] \times 10^3 \quad (3)$$

In terrestrial samples, which do not have any nucleosynthetic isotopic anomalies, the reported  $\delta^{44/40}\text{Ca}$ -value includes both the effects of natural isotopic fractionation and  $^{40}\text{Ca}$  excess due to radioactive  $^{40}\text{K}$  decay. In the case that the variations in both  $^{44}\text{Ca}/^{40}\text{Ca}$  and  $^{44}\text{Ca}/^{42}\text{Ca}$  are only due to isotopic fractionation, i.e., there is no radiogenic  $^{40}\text{Ca}$  contribution compared to NIST SRM 915a, they have the following simple relationship:

$$\delta^{44/40}\text{Ca} = 2.05 \times \delta^{44/42}\text{Ca} \quad (4)$$

where the coefficient of 2.05 represents the slope of the mass-dependent fractionation following the exponential law (Farkaš et al., 2011).

We use mass-independent Ca isotopic effects to measure the nucleosynthetic isotopic anomalies in extraterrestrial materials, such as refractory inclusions and chondrites (e.g., Simon et al., 2009; Chen et al., 2011; Lee et al., 2011). In this case, the  $^{40}\text{Ca}/^{44}\text{Ca}$ ,  $^{43}\text{Ca}/^{44}\text{Ca}$  and  $^{48}\text{Ca}/^{44}\text{Ca}$

ratios of the samples and the standard are internally normalized (indicated by N) to  $^{42}\text{Ca}/^{44}\text{Ca} = 0.31221$  (Russell et al., 1978) using an exponential law to correct for both instrumental fractionation and fractionation intrinsic to the sample. The data are reported using the  $\epsilon$  notation ( $\epsilon^{40/44}\text{Ca}$ ,  $\epsilon^{43/44}\text{Ca}$  and  $\epsilon^{48/44}\text{Ca}$ ) relative to the isotopic ratios (after internal normalization to  $^{42}\text{Ca}/^{44}\text{Ca} = 0.31221$ ) of NIST SRM 915a:

$$\epsilon^{40/44}\text{Ca} = \left[ \frac{\left( \frac{^{40}\text{Ca}}{^{44}\text{Ca}} \right)_{\text{sample(N)}}}{\left( \frac{^{40}\text{Ca}}{^{44}\text{Ca}} \right)_{\text{SRM 915a(N)}}} - 1 \right] \times 10^4 \quad (5)$$

$$\epsilon^{43/44}\text{Ca} = \left[ \frac{\left( \frac{^{43}\text{Ca}}{^{44}\text{Ca}} \right)_{\text{sample(N)}}}{\left( \frac{^{43}\text{Ca}}{^{44}\text{Ca}} \right)_{\text{SRM 915a(N)}}} - 1 \right] \times 10^4 \quad (6)$$

$$\epsilon^{48/44}\text{Ca} = \left[ \frac{\left( \frac{^{48}\text{Ca}}{^{44}\text{Ca}} \right)_{\text{sample(N)}}}{\left( \frac{^{48}\text{Ca}}{^{44}\text{Ca}} \right)_{\text{SRM 915a(N)}}} - 1 \right] \times 10^4 \quad (7)$$

Observed  $\epsilon^{40/44}\text{Ca}$  may also be due to  $^{40}\text{K}$  decay, but such effects are likely insignificant in refractory inclusions as they have extremely low K/Ca ratios. The  $^{42}\text{Ca}/^{44}\text{Ca}$ -normalization was chosen because, in general, there are no nucleosynthetic isotopic anomalies on  $^{42}\text{Ca}$  or  $^{44}\text{Ca}$  (e.g., Jungck et al., 1984; Niederer and Papanastassiou, 1984; Simon et al., 2009; Lee et al., 2011). Note, however, that Chen et al. (2011) recently reported an example of nucleosynthetic isotopic anomalies on  $^{42}\text{Ca}$  and  $^{44}\text{Ca}$  in Murchison leachates. In case there is nucleosynthetic anomaly on  $^{42}\text{Ca}$  or  $^{44}\text{Ca}$ , it is reflected in variations in all three mass-independent Ca isotopic variations ( $\epsilon^{40/44}\text{Ca}$ ,  $\epsilon^{43/44}\text{Ca}$  and  $\epsilon^{48/44}\text{Ca}$ ) because of the  $^{42}\text{Ca}/^{44}\text{Ca}$  internal normalization. If nucleosynthetic anomalies occur on  $^{42}\text{Ca}$  and  $^{44}\text{Ca}$  only, then we have the following relationship:

$$\epsilon^{48/44}\text{Ca} \approx -4\epsilon^{43/44}\text{Ca} \approx -\epsilon^{40/44}\text{Ca} \quad (8)$$

It is important to note that the isotopic ratios we report here are determined as (i) the  $\delta$ -values by double spiking – by combining data from both double-spiked and unspiked



measurements, the ratios are corrected for instrumental fractionation but not for the fractionation in nature. Note that, in our approach, the  $\delta$ -values are reported relative to a standard, but differences in  $\delta$ -values are absolute, and (ii) the  $\epsilon$ -values – corrected for both natural and instrumental fractionation using unspiked measurements. As discussed by Niederer et al. (1985), there is no unique way to split absolute isotopic variations into mass-dependent and mass-independent effects. Here we show that the reported  $\delta$ -values from the double-spiked measurements fit perfectly with the exponential fractionation law and are therefore referred to in this paper as *mass-dependent effects* – consistent with commonly used terminology. The mass-fractionation-corrected isotopic effects ( $\epsilon$ -values) are referred to as *mass-independent variations*, also consistent with commonly used terminology.

### 3.2.2. Unspiked Ca isotopic measurements

An aliquot containing  $\sim 20 \mu\text{g}$  Ca was taken from the sample solution, and Ca was separated from the sample solution using a Teflon micro-column filled with  $250 \mu\text{L}$  cation exchange resin BioRad AG50W-X12. The column chemistry was carefully calibrated to ensure 100% Ca yield, and it is described in the Appendix of Huang et al. (2010). Each sample was purified twice in order to ensure that the final Ca cut is free of matrix elements, especially K and Ti.

Ca isotopic ratios were measured at Harvard University using a GV Isoprobe-T TIMS. About  $5 \mu\text{g}$  purified Ca was loaded as calcium nitrate onto one of the side filaments of a zone refined Re triple filament assembly. We did not use  $\text{H}_3\text{PO}_4$  in our Ca loading, because we found that the in-run instrumental fractionation of Ca phosphate loading was much larger than that of Ca nitrate loading. The Ca isotopic ratios were determined using a two-sequence method. The first sequence collects masses  $^{40}\text{Ca}$ ,  $^{41}\text{K}$ ,  $^{42}\text{Ca}$ ,  $^{43}\text{Ca}$  and  $^{44}\text{Ca}$  with mass 41 in the axial cup, and the second  $^{44}\text{Ca}$  and  $^{48}\text{Ca}$  with mass 44 in the axial cup. There are several possible isobaric interferences on Ca isotopes:  $^{40}\text{K}^+$  on  $^{40}\text{Ca}^+$ ,  $^{27}\text{Al}^{16}\text{O}^+$  on  $^{43}\text{Ca}^+$ ,  $^{88}\text{Sr}^{++}$  on  $^{44}\text{Ca}^+$  and  $^{48}\text{Ti}^+$  on  $^{48}\text{Ca}^+$ . Although our column chemistry is capable of effective separation of K from Ca, there is always some K on the loaded filament assembly likely due to the post column chemistry handling. Isobaric interference of  $^{40}\text{K}$  on  $^{40}\text{Ca}$  was corrected online using  $^{40}\text{K}/^{41}\text{K} = 1.7384 \times 10^{-3}$ . During our typical isotopic measurements, the  $^{40}\text{Ca}$  beam intensity was kept at about 8 V because the maximum beam intensity allowed by our Faraday cups is 10 V. The  $^{41}\text{K}$  beam intensity was less than 0.05 V in all our analyzed samples, and less than 0.01 V in most samples. Consequently,  $^{40}\text{K}$  correction on  $^{40}\text{Ca}$  was less than 10 ppm, much smaller than our analytical errors. The mass range from 39 to 49 was carefully scanned before and after data collection using Faraday cups. No  $^{47}\text{Ti}$ ,  $^{49}\text{Ti}$  or doubly charged  $^{87}\text{Sr}$  peaks were observed in any of our analyzed samples. Since  $\text{Al}^{3+}$  can be effectively separated from  $\text{Ca}^{2+}$  on a cation column, and the extremely low oxide formation rate in our triple Re-filament assemblage, the possible  $^{27}\text{Al}^{16}\text{O}^+$  interference on  $^{43}\text{Ca}^+$  was negligible in our Ca isotopic measurements. Ca peaks and baselines were carefully examined, and no reflected ions were found in our measurements. Before each

block, baselines of all Faraday cups were collected for 30 s by positioning the central cup at mass 46.5. Each analysis consisted of 20 blocks, 10 cycles each, using 6 s integration time for each sequence, followed by 1 s waiting time. The in-run instrumental isotopic fractionation of  $^{44}\text{Ca}/^{40}\text{Ca}$  was typically less than 0.5‰. The total procedural Ca blank was less than 25 ng.

After internal normalization to  $^{42}\text{Ca}/^{44}\text{Ca}$  of 0.31221 (Russell et al., 1978), 18 measurements of NIST SRM 915a yield  $^{40}\text{Ca}/^{44}\text{Ca}$  of  $47.134 \pm 0.002$  ( $2\sigma_m$ ),  $^{43}\text{Ca}/^{44}\text{Ca}$  of  $0.064946 \pm 0.000005$  ( $2\sigma_m$ ) and  $^{48}\text{Ca}/^{44}\text{Ca}$  of  $0.088689 \pm 0.000006$  ( $2\sigma_m$ ).  $^{46}\text{Ca}$  was not determined in this study because of its low abundance. The mass-independent isotopic effects ( $\epsilon^{4i/44}\text{Ca}$ ) of measured samples are reported relative to these internal normalized  $^{4i}\text{Ca}/^{44}\text{Ca}$  values of NIST SRM 915a (Eqs. (5)–(7)), and are reported in Table 1. Each sample was analyzed multiple times, and the analytical uncertainty is expressed as two standard errors ( $2\sigma_m$ ). Specifically, the errors of the internal normalized  $^{4i}\text{Ca}/^{44}\text{Ca}$  values of NIST SRM 915a were not propagated into the reported errors of the samples.

### 3.2.3. Spiked Ca isotopic measurements

An aliquot of sample solution containing  $\sim 20 \mu\text{g}$  Ca was mixed with an appropriate amount of the  $^{43}\text{Ca}$ – $^{48}\text{Ca}$  double spike solution, so that the  $^{40}\text{Ca}/^{48}\text{Ca}$  (sample to spike ratio) of the spiked sample is between 30 and 80. This range of sample to spike ratios is optimal for determining the mass-dependent Ca isotopic effects (Huang et al., 2010). The spiked sample solution was then dried down, and dissolved in  $40 \mu\text{L}$  2.5 N HCl. Ca was purified from the spiked solution and, then, measured for Ca isotopic ratios using the GV Isoprobe-T TIMS following the procedure described above.

The mass-dependent Ca isotopic effects (Eqs. (1)–(3)) were determined by a  $^{43}\text{Ca}$ – $^{48}\text{Ca}$  double spiking technique using an offline data reduction procedure with an exponential law (Russell et al., 1978; Heuser et al., 2002; Farkaš et al., 2007a,b, 2011; Huang et al., 2010), an approach adopted from earlier Ba isotopic measurements of meteorites (Eugster et al., 1969). The  $^{43}\text{Ca}$ – $^{48}\text{Ca}$  double spike solution used in this study was prepared from isotopically enriched carbonates, Ca43-NX and Ca48-RT, from Oak Ridge National Laboratory, as described in the Appendix of Huang et al. (2010). Its isotopic composition was determined by a triple-filament TIMS technique described above assuming no instrumental fractionation, and it is reported in the Appendix of Huang et al. (2010). This implies that the isotopic composition of our  $^{43}\text{Ca}$ – $^{48}\text{Ca}$  double spike is not absolute; it is not corrected for the potential instrumental fractionation in triple-filament TIMS measurements. If the absolute isotopic composition of a double spike or a standard is available, the  $^{43}\text{Ca}$ – $^{48}\text{Ca}$  double spike technique is able to determine the absolute Ca isotopic composition of unknown samples. However, to our knowledge, there is no such Ca standard or double spike whose absolute Ca isotopic composition is known, including the  $^{42}\text{Ca}$ – $^{48}\text{Ca}$  double spike used by Niederer and Papanastassiou (1984). Therefore, in our approach we can only measure precisely the  $\delta$ -values relative to a standard sample, in this case NIST

SRM 915a (Eqs. (1)–(3)). The combined unspiked and spiked analyses of NIST SRM 915a yield  $^{40}\text{Ca}/^{44}\text{Ca}$  of  $46.406 \pm 0.001$  ( $2\sigma_m$ ),  $^{42}\text{Ca}/^{44}\text{Ca}$  of  $0.30985 \pm 0.00001$  ( $2\sigma_m$ ),  $^{43}\text{Ca}/^{44}\text{Ca}$  of  $0.064703 \pm 0.000006$  ( $2\sigma_m$ ) and  $^{48}\text{Ca}/^{44}\text{Ca}$  of  $0.089958 \pm 0.000006$  ( $2\sigma_m$ ). Note that, these values are different from those obtained by unspiked measurements in which an internal normalization to  $^{42}\text{Ca}/^{44}\text{Ca}$  of 0.31221 was applied. These values, obtained using both spiked and unspiked measurements, are not absolute isotopic compositions either, because the isotopic composition of our  $^{43}\text{Ca}$ – $^{48}\text{Ca}$  double spike contains uncorrected instrumental fractionation. Nevertheless, these values were used to calculate the  $\delta$ -values of unknown samples (Eqs. (1)–(3)). This is because the unknown samples were analyzed and their data were processed the same way as the standard sample, NIST SRM 915a. The measured  $^{4i}\text{Ca}/^{44}\text{Ca}$  are all relative to the chosen value for  $^{43}\text{Ca}/^{48}\text{Ca}$  ratio in the double spike solution, but the differences in  $\delta$ -values are absolute and independent of the  $^{43}\text{Ca}/^{48}\text{Ca}$  ratio in the double spike solution. The analytical uncertainty (two standard errors,  $2\sigma_m$ ) was estimated based on multiple measurements (Table 1). The long-term external reproducibilities of  $\delta^{44/40}\text{Ca}$  in NIST SRM 915a and IAPSO seawater are given in Fig. 1.

### 3.2.4. Reporting of Ca isotopic effects

In the Ca isotope community, mostly the low-temperature geochemistry, the mass-dependent Ca isotopic effects ( $\delta^{44/40}\text{Ca}$ ,  $\delta^{42/40}\text{Ca}$  and  $\delta^{44/42}\text{Ca}$ ) are usually reported relative to NIST SRM 915a (Hippler et al., 2003; Eisenhauer et al., 2004), despite the fact that NIST SRM 915a has been exhausted and it is now superseded by NIST SRM 915b which has a  $\delta^{44/40}\text{Ca}_{\text{SRM915a}}$  of 0.72 (Heuser and Eisenhauer, 2008). DePaolo (2004) and Simon and DePaolo (2010) argued that NIST SRM 915a and seawater have some radiogenic  $^{40}\text{Ca}$  excess compared to Earth's mantle, and

that they are therefore not suitable standard samples for reporting mass-dependent or mass-independent Ca isotopic effects. They advocated that the Ca isotopic effects be reported relative to the bulk silicate Earth (BSE). However, several recent studies show that at a  $2\sigma$  level of 0.5  $\epsilon$  units, NIST SRM 915a and seawater do *not* show any measurable radiogenic  $^{40}\text{Ca}$  excess compared to the Earth's mantle (e.g., Amini et al., 2009; Caro et al., 2010; Table 1). Therefore, in this study NIST SRM 915a is used as the standard sample for reporting both mass-dependent and mass-independent Ca isotopic effects (Eqs. (1)–(3), (5)–(7)). For mass-dependent Ca isotopic effects, a detailed discussion about the conversion between these two reference systems (NIST SRM 915a and BSE) is given in Huang et al. (2011), and the conversion equation is:

$$\delta^{44/40}\text{Ca}_{\text{BSE}}^{\text{sample}} = \delta^{44/40}\text{Ca}_{\text{SRM 915a}}^{\text{sample}} - \delta^{44/40}\text{Ca}_{\text{SRM 915a}}^{\text{BSE}} \quad (9)$$

where our current best estimate of  $\delta^{44/40}\text{Ca}_{\text{SRM 915a}}^{\text{BSE}}$  is  $1.05 \pm 0.04$  (Huang et al., 2010).

## 4. RESULTS

### 4.1. REE patterns

Two of the analyzed refractory inclusions, SJ103 and CGI, have typical Group I (flat) REE patterns at  $\sim 20\times$  chondritic level (Fig. 2), while the remaining four exhibit generic Group II REE patterns with some variations. SJ101 and WFG have typical normal Group II REE patterns. Specifically, they have LREEs (La, Ce, Pr, Nd and Sm) and Tm abundances at  $\sim 20\times$  chondritic level, but are variably depleted in ultrarefractory (Gd, Tb, Dy, Ho, Er and Lu) and volatile (Eu and Yb) REEs (Fig. 2). Two others, GFG and SJ102, have LREE and Tm abundances at  $\sim 100\times$  and  $4\times$  chondritic levels, respectively (Fig. 2). The variations in the ultrarefractory (Gd, Tb, Dy, Ho, Er

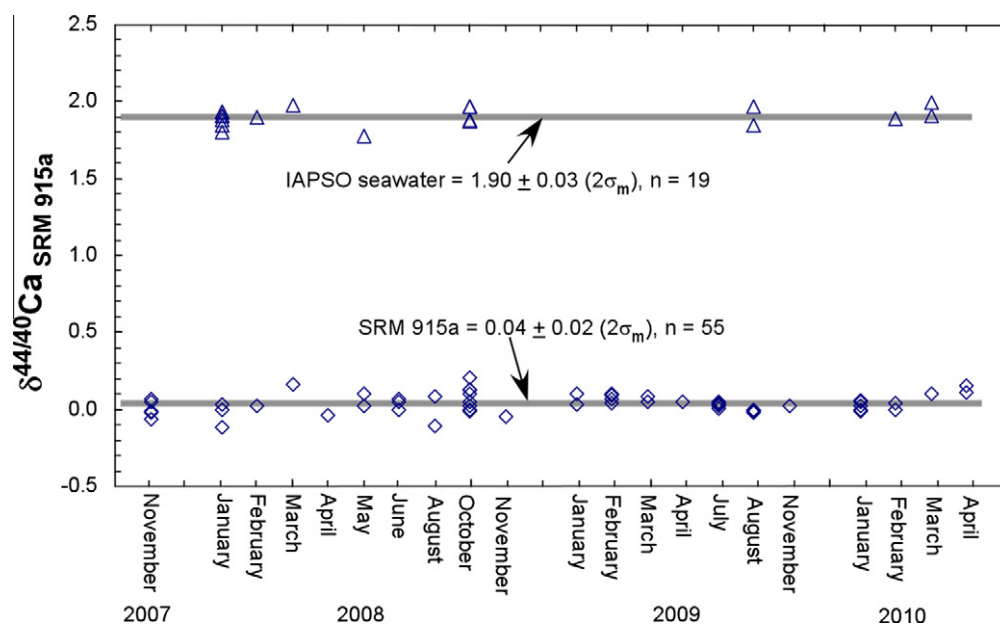


Fig. 1. The long-term  $\delta^{44/40}\text{Ca}$  reproducibility of NIST SRM 915a and IAPSO seawater obtained with the IsoProbe-T at Harvard University during the course of our study. There is no long-term  $\delta^{44/40}\text{Ca}$  drift in our measured standard samples.

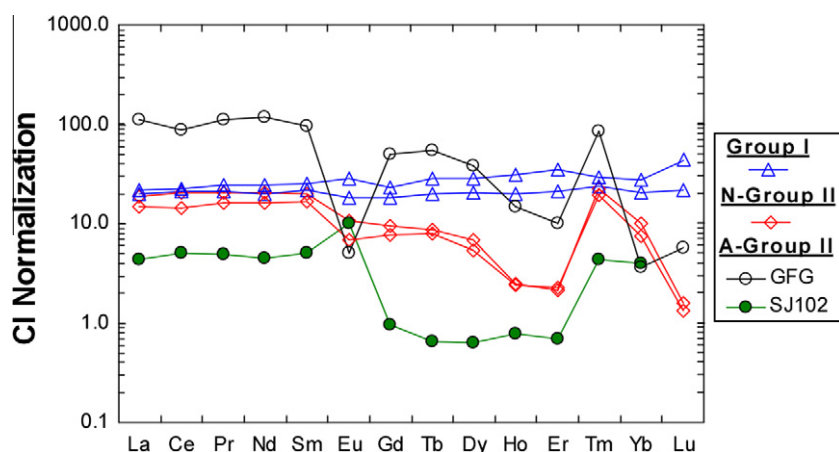


Fig. 2. CI chondrite normalized REE patterns for the six refractory inclusions studied. Two have typical Group I (flat) REE patterns, and the other four have Group II REE patterns. The N(normal)-Group II refractory inclusions have La to Sm abundances similar to those in Group I refractory inclusions, while A(anomalous)-Group II refractory inclusions exhibit either substantially higher or lower light REE abundances.

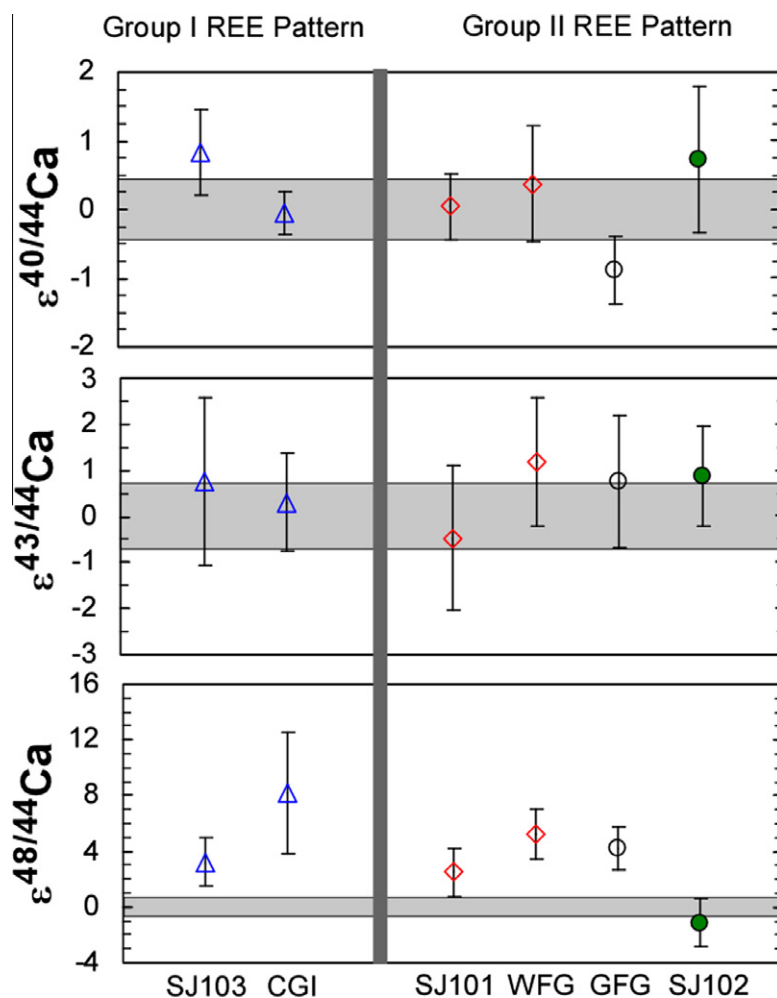


Fig. 3. Mass-independent Ca isotopic variations, normalized to  $^{42}\text{Ca}/^{44}\text{Ca} = 0.31221$  and reported using the  $\epsilon$  notation, in our studied refractory inclusions.  $\epsilon^{4i/44}\text{Ca} = [(^{4i}\text{Ca}/^{44}\text{Ca})_{\text{sample(N)}} / (^{4i}\text{Ca}/^{44}\text{Ca})_{\text{SRM 915a(N)}} - 1] \times 10,000$ . The gray bands show the  $2\sigma$  error bars of 18 measurements of NIST SRM 915a analyzed during the course of our study. Within the analytical uncertainty, there is no measurable  $^{40}\text{Ca}$  or  $^{43}\text{Ca}$  anomaly. In contrast, most studied refractory inclusions have several  $\epsilon$ -units  $^{48}\text{Ca}$  excess.

and Lu) and volatile (Eu and Yb) elements are somewhat different from those in SJ101 and WFG.

#### 4.2. Mass-independent (mass-fractionation-corrected) Ca isotopic effects ( $\epsilon$ -values)

The  $\epsilon^{40/44}\text{Ca}$  in six refractory inclusions ranges from  $-0.9 \pm 0.5$  (GFG) to  $0.8 \pm 0.6$  (SJ103), which are indistinguishable from the NIST SRM 915a ( $0.00 \pm 0.44$ ,  $n = 18$ ); and  $\epsilon^{43/44}\text{Ca}$  ranges from  $-0.5 \pm 1.6$  (SJ101) to  $1.2 \pm 1.4$  (WFG), also indistinguishable from the NIST SRM 915a ( $0.0 \pm 0.7$ ,  $n = 18$ ) (Table 1; Fig. 3). In contrast, five out of six analyzed refractory inclusions exhibit measurable  $^{48}\text{Ca}$  excess (Table 1; Fig. 3). With the exception of SJ102 ( $\epsilon^{48/44}\text{Ca} = -1.1 \pm 1.7$ ), the other five refractory inclusions studied have positive  $\epsilon^{48/44}\text{Ca}$  ranging from  $2.5 \pm 1.7$  (SJ101) to  $8.2 \pm 4.4$  (CGI), which are well resolved from the NIST SRM 915a value of  $0.0 \pm 0.7$  ( $n = 18$ ). For comparison, clinopyroxene separates from the San Carlos and Kilbourne Hole peridotites and the USGS basalt standard sample BCR-1 do not show any measurable variations in  $\epsilon^{40/44}\text{Ca}$ ,  $\epsilon^{43/44}\text{Ca}$  or  $\epsilon^{48/44}\text{Ca}$  (Table 1).

#### 4.3. Mass-dependent Ca isotopic effects ( $\delta$ -values)

All analyzed refractory inclusions have  $\delta^{44/40}\text{Ca}$  lower than the estimated  $\delta^{44/40}\text{Ca}$  of the bulk silicate Earth ( $\delta^{44/40}\text{Ca} = 1.05$ ; DePaolo, 2004; Amini et al., 2009; Huang et al., 2010; Simon and DePaolo, 2010) (Fig. 4). They exhibit large variations in  $\delta^{44/40}\text{Ca}$ ,  $\delta^{44/42}\text{Ca}$  and  $\delta^{42/40}\text{Ca}$  (Table 1; Fig. 4). For example,  $\delta^{44/40}\text{Ca}$  ranges from

$-5.60 \pm 0.05$  (GFG) to  $0.35 \pm 0.02$  (CGI). Importantly, all six refractory inclusions plot on the exponential fractionation trends in the three Ca-isotope plots ( $\delta^{44/40}\text{Ca}$  vs.  $\delta^{44/42}\text{Ca}$  and  $\delta^{42/40}\text{Ca}$ ) (Fig. 4), implying that there are no detectable nucleosynthetic anomalies in  $^{40}\text{Ca}$ ,  $^{42}\text{Ca}$  or  $^{44}\text{Ca}$ , consistent with the observed mass-independent Ca isotopic effects (Fig. 3).

## 5. DISCUSSION

### 5.1. Nucleosynthetic anomalies in Ca isotopes

At  $2\sigma$  levels of  $\pm 0.5$  and  $\pm 1.5$  for  $\epsilon^{40/44}\text{Ca}$  and  $\epsilon^{43/44}\text{Ca}$ , respectively, our data show no measurable  $^{40}\text{Ca}$  or  $^{43}\text{Ca}$  anomalies in all six refractory inclusions (Table 1; Fig. 3). Nevertheless, five out of six analyzed inclusions exhibit  $^{48}\text{Ca}$  excesses clearly resolved from the terrestrial standard (Table 1; Fig. 3). These results are consistent with the previous work (Jungck et al., 1984; Niederer and Papanastassiou, 1984), who also observed  $^{48}\text{Ca}$  excess and no  $^{40}\text{Ca}$  or  $^{43}\text{Ca}$  anomalies in refractory inclusions from Allende and Leoville. In contrast, Simon et al. (2009) reported up to  $2\epsilon$  units  $^{40}\text{Ca}$  excess in two refractory inclusions from Allende, and a subsequent study reported that these two refractory inclusions also have  $^{48}\text{Ca}$  excess (Moynier et al., 2010). The level of  $^{40}\text{Ca}$  excess reported by Simon et al. (2009) well exceeds the analytical uncertainty of  $\epsilon^{40/44}\text{Ca}$  in our study, as well as those of Jungck et al. (1984) and Niederer and Papanastassiou (1984). Therefore, if the  $^{40}\text{Ca}$  excess observed in two refractory inclusions reported by Simon et al. (2009) is not an analytical artifact, it

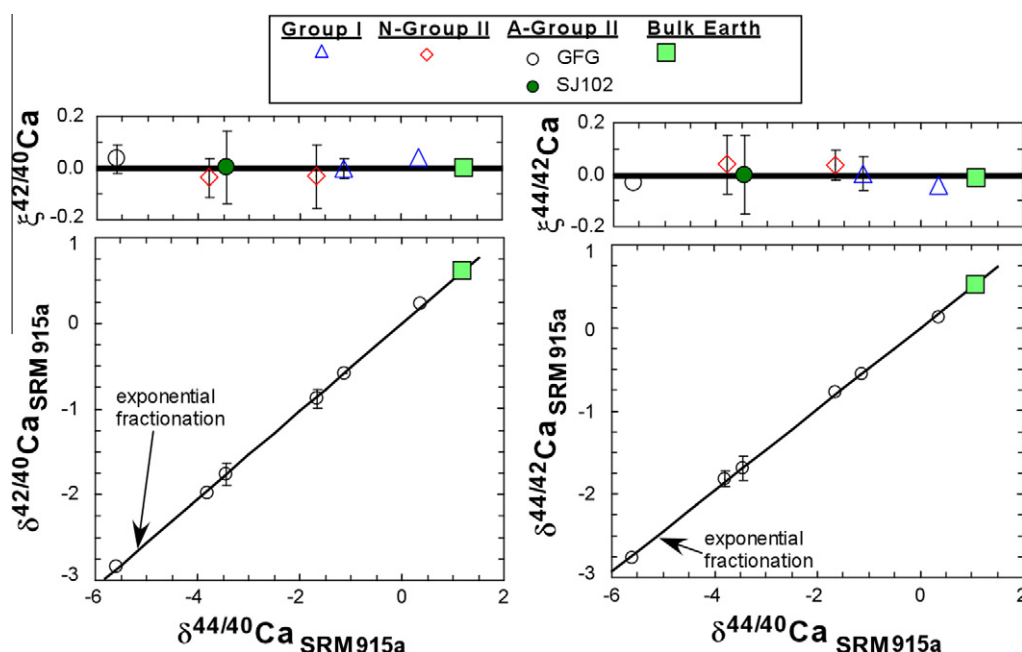


Fig. 4.  $\delta^{44/40}\text{Ca}$  vs.  $\delta^{42/40}\text{Ca}$  and  $\delta^{44/42}\text{Ca}$  in the refractory inclusions studied. Error bars smaller than the symbols are not shown. Bulk Earth estimates from Huang et al. (2010), which are similar to that of Simon and DePaolo (2010), are shown for comparison. Exponential fractionation trends are shown for comparison, which are described as:  $^{i}\text{Ca}/^{j}\text{Ca} = (^{k}\text{Ca}/^{j}\text{Ca})^{\beta}$ , with  $i, j, k$  being atomic masses and  $\beta = \ln(i/j)/\ln(k/j)$ . The upper panels show the deviations (in  $\delta$ -units) from exponential fractionation trends at a given  $\delta^{44/40}\text{Ca}$ , defined as  $\xi^{42/40}\text{Ca}$  and  $\xi^{44/42}\text{Ca}$ . By definition, the exponential fractionation trends are horizontal lines in these two panels. The errors of the  $\delta$ -values are propagated into errors of the  $\xi$ -values.



implies that this type of refractory inclusions was not sampled by us and other groups (Jungck et al., 1984; Niederer and Papanastassiou, 1984; Fig. 3).

Recently, small  $^{43}\text{Ca}$  anomalies,  $\sim 0.3 \epsilon$  units of excess in  $^{43}\text{Ca}$ , were found in five refractory inclusions by Lee et al. (2011) who optimized their analytical protocol to measure  $^{43}\text{Ca}$  with the highest precision achieved so far by measuring at very high beam intensities and avoiding measuring the  $^{40}\text{Ca}$  beam. We note that this level of  $^{43}\text{Ca}$  excess is much smaller than the analytical uncertainty of our study and those of Jungck et al. (1984) and Niederer and Papanastassiou (1984).

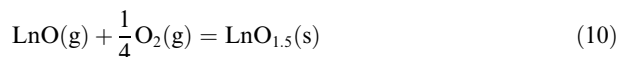
The observed  $^{48}\text{Ca}$  excess reflects a nucleosynthetic anomaly (Lee et al., 1978, 1979; Jungck et al., 1984; Niederer and Papanastassiou, 1984), and a component enriched in neutron-rich nucleosynthetic isotopes is inferred (Cameron, 1979). The widespread nucleosynthetic anomaly does not correlate with mass-dependent Ca isotopic effects or the REE abundance ratios in refractory inclusions studied.

## 5.2. Correlation between REE pattern and $\delta^{44/40}\text{Ca}$ and its implication to the origin of refractory inclusions

An important result of the present work is a clear correlation between the mass-dependent Ca isotopic fractionation of the refractory inclusions studied and their REE patterns that was not reported in previous isotopic studies of CAIs. Because large isotopic fractionations occur typically in non-equilibrium, kinetically controlled processes, the lack of correlation between the isotopic and chemical fractionations in a refractory inclusion is merely an indication that at some point isotopic and chemical fractionations were decoupled from each other, perhaps when chemical evolution of the system has reached a near-equilibrium path. Given a complicated nebular history of refractory inclusions involving multiple episodes of evaporation and condensation, the decoupling of isotopic and chemical fractionations is very likely and, in fact, expected. However, when preserved, the correlated chemical and isotopic fractionations provide a powerful tool for deciphering condensation and evaporation history of a nebular object (e.g., Richter, 2004; Richter et al., 2002; Grossman et al., 2008). Here we use the observed correlation of  $\delta^{44/40}\text{Ca}$  with the REE patterns of the inclusions studied to evaluate origin of the Group II REE pattern that cannot be done based on REE abundance pattern alone.

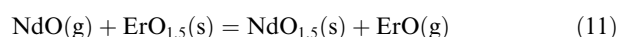
The distinctive Group II REE pattern, first recognized in the pink portion of a CAI from Allende by Tanaka and Masuda (1973), is characterized by an enrichment of Tm relative to its neighbors, Er and Yb. Its origin is thought to be related to the REE elemental fractionation according to their relative volatility during high temperature evaporation and condensation processes (e.g., Boynton, 1975; Davis and Grossman, 1979). Boynton (1975) was the first to provide a theoretical interpretation of the distinctive Group II REE pattern using the thermodynamic data available at that time, which was followed by Davis and Grossman (1979). We use the conceptual model from these papers to understand the new REE and Ca isotopic data presented in this paper.

During condensation, the relative volatility of each REE is a function of  $f_{\text{O}_2}$  in the solar nebula. Most REEs are monoxides in the nebula (La, Pr, Nd, Sm, Gd, Tb, Dy, Er and Lu) so the condensation reactions for these REEs (Ln) are:



where “g” and “s” represent gaseous and solid phases, respectively.

La, Pr, Nd and Sm are known to have similar volatilities, while elements from Gd to Lu get systematically more refractory. Increasing  $f_{\text{O}_2}$  would make these elements more refractory, but it should not change their relative volatilities as  $f_{\text{O}_2}$  is canceled out in exchange reactions. For example for Nd and Er we obtain the following exchange reaction:



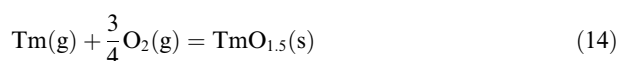
In the case of an ideal mixing of the REE oxides in a solid we have the following simple relationship between the thermodynamic equilibrium constant and the Nd/Er-ratio in the condensed solid and gas:

$$K^{\text{Nd-Er}} = \frac{x_{\text{NdO}_{1.5}}^{\text{solid}} x_{\text{ErO}}^{\text{gas}}}{x_{\text{ErO}_{1.5}}^{\text{solid}} x_{\text{NdO}}^{\text{gas}}} = \frac{\left(\frac{\text{Nd}}{\text{Er}}\right)_{\text{solid}}}{\left(\frac{\text{Nd}}{\text{Er}}\right)_{\text{gas}}} \quad (12)$$

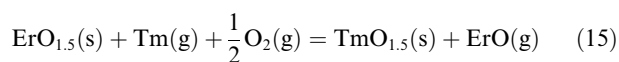
or

$$\left(\frac{\text{Nd}}{\text{Er}}\right)_{\text{solid}} = K^{\text{Nd-Er}} \left(\frac{\text{Nd}}{\text{Er}}\right)_{\text{gas}} \quad (13)$$

The elements Ce, Eu, Tm and Yb are exceptions, because they are involved in more complicated exchange equilibria that are  $f_{\text{O}_2}$  dependent due to multiple oxidation states in either the gaseous or condensed phases, or both (e.g., Boynton, 1975; Davis and Grossman, 1979). In particular, we are interested in the Tm anomaly of the REE pattern. Under normal nebular conditions, Tm in the gaseous phase is primarily monatomic, so its condensation is described by following condensation reaction:



Then the Tm–Er exchange reaction is:



The equilibrium constant for the Tm–Er exchange between the gaseous and solid phases is:

$$K^{\text{Tm-Er}} = \frac{x_{\text{TmO}_{1.5}}^{\text{solid}} x_{\text{ErO}}^{\text{gas}}}{x_{\text{ErO}_{1.5}}^{\text{solid}} x_{\text{Tm}}^{\text{gas}} (f_{\text{O}_2})^{1/2}} = \frac{\left(\frac{\text{Tm}}{\text{Er}}\right)_{\text{solid}}}{\left(\frac{\text{Tm}}{\text{Er}}\right)_{\text{gas}}} (f_{\text{O}_2})^{-1/2} \quad (16)$$

or

$$\left(\frac{\text{Tm}}{\text{Er}}\right)_{\text{solid}} = \left(\frac{\text{Tm}}{\text{Er}}\right)_{\text{gas}} (f_{\text{O}_2})^{1/2} K^{\text{Tm-Er}} \quad (17)$$

In more oxidized environments, there will be increasing amounts of TmO in the gaseous phase, leading to a change in the exponent for  $f_{\text{O}_2}$  in Eq. (17). If all Tm in the gas is present as TmO, then the Tm–Er exchange reaction is similar to that of Nd–Er exchange reaction (Eq. (11)).

Consequently, the dependence on  $f_{O_2}$  disappears and Tm will behave very similarly to Er. Further, fractionation of Tm from other heavy REEs, such as Er, occurs only at a reducing environment with the presence of Tm(g) and HREE oxides (g), such as ErO, as required by the Tm–Er exchange reaction (Eq. (15)). This environment is typical of the solar nebula. Such fractionation is not observed in evaporation experiments (Davis and Hashimoto, 1995; Davis et al., 1995, 1999), presumably due to the different conditions in their experiments.

Refractory inclusions with Group II REE patterns are thought to be condensates from a fractionated nebular reservoir with a similar pattern (e.g., Boynton, 1975; Davis and Grossman, 1979). It was suggested that such a reservoir was formed by segregation of a high temperature phase containing the most refractory REEs (i.e., characterized by an ultrarefractory REE pattern, Boynton et al., 1980; Ireland et al., 1988; Simon et al., 1996, 2002; El Goresy et al., 2002; Hiyagon et al., 2003) from a gas of solar composition. Subsequent con-

densation of the remaining REEs except for the most volatile ones (Eu and Yb) resulted in the Group II pattern. The high temperature phase hosting ultrarefractory REEs was originally proposed to be perovskite (Davis and Grossman, 1979), but later it was changed to hibonite (MacPherson and Davis, 1994). The ultrarefractory REE patterns identified in some Murchison and Allende CAIs have unusually low Nd/Er and Tm/Er ratios (Boynton et al., 1980; Ireland et al., 1988; Simon et al., 1996, 2002; El Goresy et al., 2002; Hiyagon et al., 2003). Thus, these ratios are excellent “tracers or monitors” of the removed ultrarefractory REE component. The advantage of the Nd/Er ratio is its independence on the  $f_{O_2}$  in the nebula and, therefore, on the C/O ratio of the nebula. Such fractionation could have occurred upon the infall of molecular cloud material to the nebula, or during local high-temperature excursions in the CAI formation regions(s) as suggested by the presence of refractory nodules with different REE patterns in a single CAI (e.g., Hiyagon et al., 2003).

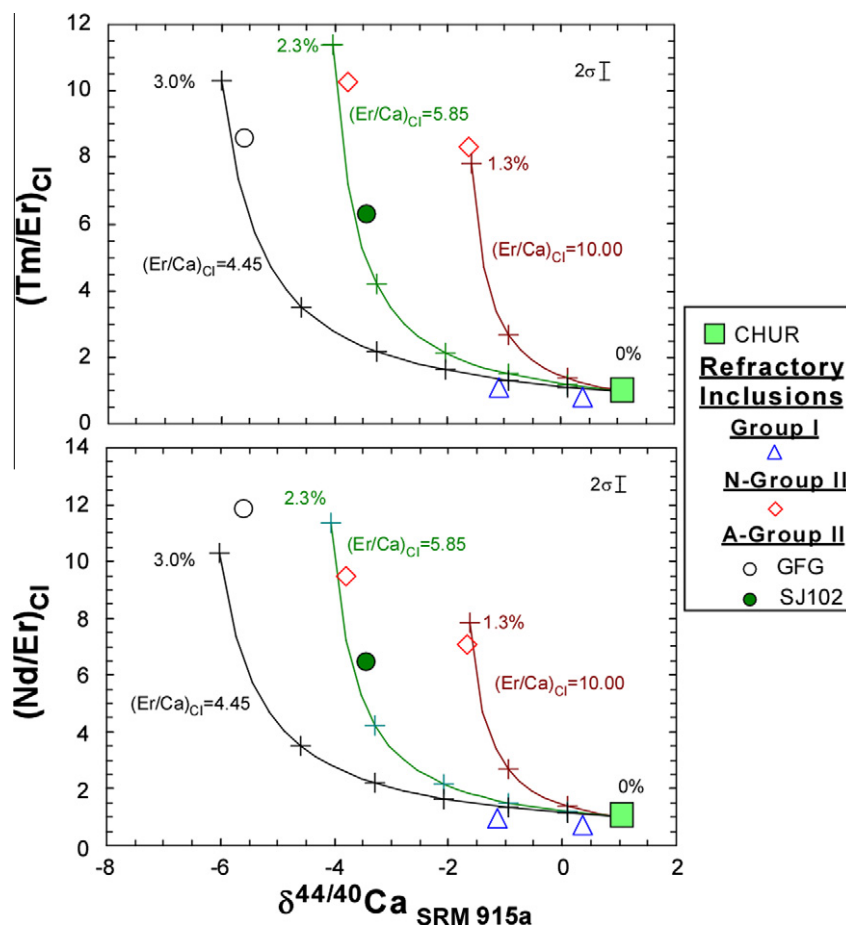


Fig. 5. The relationship between the  $\delta^{44/40}\text{Ca}$ ,  $(\text{Tm}/\text{Er})_{\text{CI}}$  and  $(\text{Nd}/\text{Er})_{\text{CI}}$  ratios in the inclusions studied. The analytical error on  $\delta^{44/40}\text{Ca}$  is smaller than the symbols, and the typical analytical errors on Tm/Er and Nd/Er are shown in the upper right corner. The subscript CI denotes CI chondrite normalized values. The model lines show the evolution of  $\delta^{44/40}\text{Ca}$ ,  $(\text{Tm}/\text{Er})_{\text{CI}}$  and  $(\text{Nd}/\text{Er})_{\text{CI}}$  ratios after segregation of different amounts of an ultrarefractory evaporation residue from a chondritic reservoir (CHUR) with the Earth-like  $\delta^{44/40}\text{Ca}$  of +1.05 (Huang et al., 2010). The ultrarefractory evaporation residue is assumed to have CaO of 9% and  $\delta^{44/40}\text{Ca}$  of +28 (similar to the HAL hibonites; Lee et al., 1979; Ireland et al., 1992), and both  $(\text{Tm}/\text{Er})_{\text{CI}}$  and  $(\text{Nd}/\text{Er})_{\text{CI}}$  ratio of 0.25 (El Goresy et al., 2002; Hiyagon et al., 2003). Three curves with different  $(\text{Er}/\text{Ca})_{\text{CI}}$  ratios in the ultrarefractory evaporation residue are shown. The tick marks on the curves show the amounts of the ultrarefractory residue (wt.%), with 0.5% increments, segregated from a CHUR reservoir.

However, it is still unclear whether such a high temperature phase was an evaporation residue or a condensate. In principle, mass-dependent isotopic variations can be used to distinguish between these two scenarios. In a kinetically controlled process, an evaporation residue would be enriched in heavy isotopes (e.g., Ireland et al., 1992; Simon and DePaolo, 2010), while a condensate tends to be enriched in light isotopes until an element is fully condensed (e.g., Richter, 2004; Simon and DePaolo, 2010). For example, very heavy Ca isotopes have been found in HAL-type hibonites from the CV3 Allende, H3 Dhajala and CM2 Murchison chondrites (Lee et al., 1979; Hinton et al., 1988; Ireland et al., 1992), which were thought to represent evaporation residues. Therefore, if the Group II REE pattern is formed by segregation of an evaporation residue, the Group II REE pattern should be coupled with lighter Ca isotopes. Alternatively, if the ultrarefractory component is a condensate, it is isotopically light and the Group II REE pattern should be accompanied by heavier Ca isotopes.

Among six inclusions studied, two have Group I REE patterns, and four have Group II REE patterns (Fig. 2). The refractory inclusions with Group II REE patterns have lighter Ca isotopes than those with Group I REE patterns. Specifically, our data show negative correlations between  $\delta^{44/40}\text{Ca}$ ,  $(\text{Tm}/\text{Er})_{\text{CI}}$  and  $(\text{Nd}/\text{Er})_{\text{CI}}$  (the subscript CI denotes CI chondrite normalization), with  $R^2$  of 0.60 and 0.84, respectively (Fig. 5).

It is well known that inter-mineral fractionation cannot generate the Group II REE pattern (e.g., Table 1 of Beckett et al., 2006). Although Ca isotopes may be fractionated among different rock-forming minerals, such as orthopyroxene and clinopyroxene (Huang et al., 2010), the inter-mineral Ca isotopic fractionation is much smaller, less than 1‰ in  $^{44}\text{Ca}/^{40}\text{Ca}$ , compared to the observed  $\delta^{44/40}\text{Ca}$  variation within our analyzed refractory inclusions (from  $-5.60$  to  $+0.35$ ; Figs. 4 and 5). It appears that the large, correlated isotopic-elemental fractionation effects ( $\delta^{44/40}\text{Ca}$  vs.  $\text{Tm}/\text{Er}$  and  $\text{Nd}/\text{Er}$ ) must reflect the primary formation process.

The negative  $\delta^{44/40}\text{Ca}-(\text{Tm}/\text{Er})_{\text{CI}}$  and  $\delta^{44/40}\text{Ca}-(\text{Nd}/\text{Er})_{\text{CI}}$  trends in Fig. 5 are inconsistent with formation of the Group II REE pattern by segregation of a high temperature condensate. Therefore, we prefer to explain the observed correlation between Ca isotopes and REE patterns (Fig. 5) by incomplete evaporation of the dust as this mechanism is capable of producing large fractionations in Ca isotopes with very high  $\delta^{44/40}\text{Ca}$  in the residual refractory grains (e.g., Mason and Taylor, 1982; Niederer and Papanastassiou, 1984). In order to explain the observed negative  $\delta^{44/40}\text{Ca}-(\text{Tm}/\text{Er})_{\text{CI}}$  and  $\delta^{44/40}\text{Ca}-(\text{Nd}/\text{Er})_{\text{CI}}$  trends (Fig. 5), we propose the following narrative scenario:

1. A high-temperature heating event almost completely vaporized a portion of the solar nebula, leaving behind a small amount of an ultrarefractory residue, characterized by high  $\delta^{44/40}\text{Ca}$  and low  $(\text{Tm}/\text{Er})_{\text{CI}}$  and  $(\text{Nd}/\text{Er})_{\text{CI}}$ . The coexisting vapor phase is characterized by low  $\delta^{44/40}\text{Ca}$  and a Group II REE pattern, i.e., high  $(\text{Tm}/\text{Er})_{\text{CI}}$  and  $(\text{Nd}/\text{Er})_{\text{CI}}$ .

2. Subsequent condensation of the vapor phase at a lower temperature produced refractory inclusions or their precursors. The refractory inclusions that accreted both the condensate and the ultrarefractory residue ended up with a flat REE pattern, i.e., Group I REE pattern, and a chondritic Ca isotopic composition. If the ultrarefractory residue was not accreted, then inclusions with a Group II REE pattern coupled with light Ca isotopes were formed.

This scenario was tested by a mass-balance modeling of evolution of  $\text{Tm}/\text{Er}$  and  $\text{Nd}/\text{Er}$  ratios, and Ca isotopic compositions in a chondritic system that has lost different amounts of an ultrarefractory evaporation residue. The ultrarefractory evaporation residue was assumed to have a hibonite-like CaO content of 9%, and both  $(\text{Tm}/\text{Er})_{\text{CI}}$  and  $(\text{Nd}/\text{Er})_{\text{CI}}$  ratios of 0.25, similar to these found in the ultrarefractory nodules (e.g., Boynton et al., 1980; Ireland et al., 1988; Simon et al., 1996, 2002; El Goresy et al., 2002; Hiyagon et al., 2003). We use a  $\delta^{44/40}\text{Ca}$  of +28, as was found for HAL hibonite (Lee et al., 1979; Ireland et al., 1992; re-normalized to NIST 915a scale), but we do not imply that HAL is the missing ultrarefractory component, since HAL does not have excess  $^{26}\text{Mg}$  and an ultrarefractory REE pattern that fit our model. We simply use this  $\delta^{44/40}\text{Ca}$  as a proxy since none of the inclusions or nodules with ultrarefractory REE patterns have been analyzed for Ca isotopes. The results of modeling (Fig. 5) illustrate how the removal of an ultrarefractory residue affects the REE composition and Ca isotopic compositions of the modeled refractory inclusions or their precursors. The model calculations suggest that the observed  $\delta^{44/40}\text{Ca}-(\text{Tm}/\text{Er})_{\text{CI}}$  and  $\delta^{44/40}\text{Ca}-(\text{Nd}/\text{Er})_{\text{CI}}$  trends can be reproduced by segregation of an ultrarefractory residue, which constitute only 0.5–3 wt.% of the initial chondritic reservoir. These amounts (0.5–3%) of segregated ultrarefractory residue contain 3% to 20% of the Ca budget in the initial chondritic reservoir.

## 6. CONCLUSIONS

Our combined Ca isotopic and REE study on six refractory inclusions from Allende CV3 chondrite reveal the following important results:

1. Refractory inclusions exhibit large variations in Ca isotopes (up to 6‰ in  $^{44}\text{Ca}/^{40}\text{Ca}$ ), with all refractory inclusions studied being lighter than the bulk silicate Earth;
2. The fractionation of Ca isotopes is correlated with the magnitude of fractionation of Tm from other heavy REEs, such as Er. Specifically, the observed negative  $^{44}\text{Ca}/^{40}\text{Ca}-\text{Tm}/\text{Er}$ ,  $-\text{Nd}/\text{Er}$  trends can be explained by the segregation of 0.5–3% of an ultrarefractory evaporation residue, characterized by high  $^{44}\text{Ca}/^{40}\text{Ca}$  and low  $\text{Tm}/\text{Er}$  and  $\text{Nd}/\text{Er}$ , from a chondritic reservoir before the formation of refractory inclusions or their precursors;
3. At  $2\sigma$  levels of  $\pm 0.5$  and  $\pm 1.5$  for  $\epsilon^{40/44}\text{Ca}$  and  $\epsilon^{43/44}\text{Ca}$ , respectively, there are no detectable anomalies of  $^{40}\text{Ca}$  and  $^{43}\text{Ca}$  in the refractory inclusions studied. However,

five out of six show  $^{48}\text{Ca}$  excesses of several  $\varepsilon$  units, which are clearly resolvable from the terrestrial standard.

### ACKNOWLEDGEMENTS

This work was supported by NASA Origins of Solar Systems Program awards NNX07AI80G and NNX11AK82G, and partial support from the Harvard University Origins of Life Initiative, the Canadian Institute for Advanced Research (CIFAR), and the Faculty of Environmental Sciences (Grant No. 42900/1312/3166) are greatly acknowledged. This work benefitted greatly from discussions with G.J. Wasserburg and D.A. Papanastassiou. We thank G.J. Wasserburg, J.I. Simon and A.M. Davis for their careful and constructive reviews and D.A. Papanastassiou for his editorial handling.

### REFERENCES

- Amelin Y., Krot A. N., Hutcheon I. D. and Ulyanov A. A. (2002) Lead isotopic ages of chondrules and calcium–aluminum-rich inclusions. *Science* **297**, 1678–1683. doi:10.1126/science.1073950.
- Amelin Y., Kaltenbach A., Iizuka T., Stirling C. H., Ireland T. R., Petaev M. and Jacobsen S. B. (2010) U–Pb chronology of the Solar System's oldest solids with variable  $^{238}\text{U}/^{235}\text{U}$ . *Earth Planet. Sci. Lett.* **300**, 343–350. doi:10.1016/j.epsl.2010.10.015.
- Amini M., Eisenhauer A., Böhm F., Holmden C., Kreissig K., Hauff F. and Jochum K. P. (2009) Calcium isotopes ( $\delta^{44/40}\text{Ca}$ ) in MPI-DING reference glasses, USGS rock powders and various rocks: evidence for Ca isotope fractionation in terrestrial silicates. *Geostand. Newsl.* **33**, 231–247.
- Beckett J. R., Connolly H. C. and Ebel D. S. (2006) Chemical processes in igneous calcium–aluminum-rich inclusions: a mostly CMAS view of melting and crystallization. In *Meteorites and the Early Solar System* (ed. D. Lauretta et al.). University Arizona, Tucson, pp. 399–429.
- Birmingham K. R. and Mezger K. (2010) Ba Isotope Abundances in Equilibrated Meteorites and CAIs. *Lunar Planet. Sci.* **41**, #1735.
- Birck J. L. and Lugmair G. W. (1988) Nickel and chromium isotopes in Allende inclusions. *Earth Planet. Sci. Lett.* **90**, 131–143.
- Bogdanovski O. (1997) Development of highly-sensitive technique for Sm–Nd isotopic analysis and their application to the study of terrestrial and extraterrestrial objects. Ph.D. dissertation, der Johannes Gutenberg Universität in Mainz, pp. 146.
- Boynton W. V. (1975) Fractionation in the solar nebula: condensation of yttrium and the rare earth elements. *Geochim. Cosmochim. Acta* **39**, 569–584.
- Boynton W. V. (1984) Cosmochemistry of the rare earth elements: meteorite studies. In *Rare Earth Element Geochemistry* (ed. P. Henderson). Elsevier, Amsterdam, pp. 63–114.
- Boynton W. V., Frazier R. M. and Macdougall J. D. (1980) Identification of an ultra-refractory component in the Murchison. *Lunar Planet. Sci.* **XI**, 103–105.
- Cameron A. G. W. (1979) The neutron-rich silicon-burning and equilibrium processes of nucleosynthesis. *Astrophys. J.* **230**, L53–L57.
- Caro G., Papanastassiou D. A. and Wasserburg G. J. (2010)  $^{40}\text{K}$ – $^{40}\text{Ca}$  isotopic constraints on the oceanic calcium cycles. *Earth Planet. Sci. Lett.* **296**, 124–132.
- Chen, J. H., Papanastassiou, D. A. and Dauphas, N. (2011) Anomalous Ca Isotopic Compositions in Leachates of Murchison. *Lunar Planet. Sci.* **42nd** #2440.
- Clayton R. N., Grossman L. and Mayeda T. L. (1973) A component of primitive nuclear composition in carbonaceous meteorites. *Science* **182**, 485–488.
- Clayton R. N., Hinton R. W. and Davis A. M. (1988) Isotopic variations in the rock-forming elements in meteorites. *Phil. Trans. R. Soc. Lond. A* **325**, 483–501.
- Connelly J. N., Amelin Y., Krot A. N. and Bizzarro M. (2008) Chronology of the solar system's oldest solids. *Astrophys. J.* **675**, L121–L124.
- Davis A. M. and Grossman L. (1979) Condensation and fractionation of rare earths in the solar nebula. *Geochim. Cosmochim. Acta* **43**, 1611–1632.
- Davis A. M. and Hashimoto A. (1995) Volatility fractionation of rare earth elements and other trace elements during vacuum evaporation. *Meteoritics* **30**, 500–501.
- Davis A. M., Hashimoto A., Clayton R. C. and Mayeda T. K. (1995) Isotopic and chemical fractionation during evaporation of  $\text{CaTiO}_3$ . *Lunar Planet. Sci.* **26**, 317–318.
- Davis A. M., Hashimoto A. and Parsad N. (1999) Trace element fractionation during evaporation in reducing atmospheres. *Lunar Planet. Sci.* **XXX**, #2023.
- DePaolo D. J. (2004) Calcium isotopic variations produced by biological, kinetic, radiogenic and nucleosynthetic processes. In *Reviews in Mineralogy and Geochemistry* (ed. Jodi Rosso), Mineralogical Society of America, 55, 255–288.
- Eisenhauer A., Nagler T., Stille P., Kramers J., Gussone N., Bock B., Fietzke J., Hippler D. and Schmitt A.-D. (2004) Proposal for an international agreement on Ca notation as a result of the discussion from the workshop on stable isotope measurements in Davos (Goldschmidt 2002), Nice (EGS-AGU-EUG 2003). *Geostand. Geoanal. Res.* **28**, 149–151.
- El Goresy A., Zinner E., Matsunami S., Palme H., Spettel B., Lin Y. and Nazarov M. (2002) Efremovka 101.1: a CAI with ultrarefractory REE patterns and enormous enrichments of Sc, Zr, and Y in fassaite and perovskite. *Geochim. Cosmochim. Acta* **66**, 1459–1491.
- Eugster O., Tera F. and Wasserburg G. J. (1969) Isotopic analyses of barium in meteorites and in terrestrial samples. *J. Geophys. Res.* **74**, 3897–3908.
- Farkaš J., Buhl D., Blenkinsop J. and Veizer J. (2007a) Evolution of the oceanic calcium cycle during the late Mesozoic: evidence from  $\delta^{44/40}\text{Ca}$  of marine skeletal carbonates. *Earth Planet. Sci. Lett.* **253**, 96–111.
- Farkaš J., Böhm F., Wallmann K., Blenkinsop J., Eisenhauer A., Geldren R. V., Munnecke A., Voigt S. and Veizer J. (2007b) Calcium isotope record of Phanerozoic oceans: implications for chemical evolution of seawater and its causative mechanisms. *Geochim. Cosmochim. Acta* **71**, 5117–5134.
- Farkaš J., Déjéant A., Novák M. and Jacobsen S. B. (2011) Calcium isotope constraints on the uptake and sources of  $\text{Ca}^{2+}$  in a base-poor forest: a new concept of combining stable ( $\delta^{44/42}\text{Ca}$ ) and radiogenic ( $\varepsilon_{\text{Ca}}$ ) signals. *Geochim. Cosmochim. Acta* **75**, 7031–7046, doi:10.1016/j.gca.2011.09.021.
- Gray C. M., Papanastassiou D. A. and Wasserburg G. J. (1973) The identification of early condensates from the solar nebula. *Icarus* **20**, 213–239.
- Grossman L. and Larimer J. W. (1974) Early chemical history of the solar system. *Rev. Geophys. Space Phys.* **12**, 71–101.
- Grossman L., Simon S. B., Rai V. K., Thiemens M. H., Hutcheon I. D., Williams R. W., Galy A., Ding T., Fedkin A. V., Clayton R. N. and Mayeda T. K. (2008) Primordial compositions of refractory inclusions. *Geochim. Cosmochim. Acta* **72**, 3001–3021, doi:10.1016/j.gca.2008.04.002.



- Harper, Jr., C. L. (1993) Isotopic astronomy from anomalies in meteorites: recent advances and new frontiers. *J. Phys. G: Nucl. Part. Phys.* **19**, S81–S94.
- Heuser A., Eisenhauer A., Gussone N., Bock B., Hansen B. T. and Nagler T. F. (2002) Measurement of calcium isotopes ( $\delta^{44/40}\text{Ca}$ ) using a multicollector TIMS technique. *Int. J. Mass. Spectrom.* **220**, 387–399.
- Heuser A. and Eisenhauer A. (2008) The calcium isotope composition ( $\delta^{44/40}\text{Ca}$ ) of NIST SRM 915b and NIST SRM 1486. *Geostand. Geoanal. Res.* **32**, 311–315.
- Hinton R. W., Davis A. M. and Scatena-Wachel D. E. (1988) A chemical and isotopic study of hibonite-rich refractory inclusions in primitive meteorites. *Geochim. Cosmochim. Acta* **52**, 2573–2598.
- Hippler D., Schmitt A.-D., Gussone N., Heuser A., Stille P., Eisenhauer A. and Nagler T. F. (2003) Calcium isotopic composition of various reference materials and seawater. *Geostand. Newsl.* **27**, 13–19.
- Hiyagon, H., Hashimoto, A., Kimura, M. and Ushikubo, T. (2003) First Discovery of an Ultra-Refractory Nodule in an Allende Fine-Grained Inclusion. *Lunar Planet. Sci.* **XXXIV**, #1552.
- Huang S. and Frey F. A. (2003) Trace element abundances of Mauna Kea basalt from phase 2 of the Hawaii Scientific Drilling Project: petrogenetic implications of correlations with major element content and isotopic ratios. *Geochim. Geophys. Geosyst.* **4**(6), 8711, doi:10.1029/2002GC000322.
- Huang S., Farkaš J. and Jacobsen S. B. (2010) Calcium isotopic fractionation between clinopyroxene and orthopyroxene from mantle peridotites. *Earth Planet. Sci. Lett.* **292**, 337–344, doi:10.1016/j.epsl.2010.01.042.
- Huang S., Farkaš J. and Jacobsen S. B. (2011) Stable calcium isotopic compositions of Hawaiian shield lavas: evidence for recycling of ancient marine carbonates into the mantle. *Geochim. Cosmochim. Acta* **75**, 4987–4997, doi:10.1016/j.gca.2011.06.010.
- Ireland T. R. and Fegley B. J. R. (2000) The solar system's earliest chemistry: systematics of refractory inclusion. *Intern. Geol. Rev.* **42**, 865–894.
- Ireland T. R., Fahey A. J. and Zinner E. K. (1988) Trace-element abundances in hibonites from the Murchison carbonaceous chondrite: constraints on high-temperature processes in the solar nebula. *Geochim. Cosmochim. Acta* **52**, 2841–2854.
- Ireland T. R., Zinner E. K., Fahey A. J. and Esat T. M. (1992) Evidence for distillation in the formation of HAL and related hibonite inclusions. *Geochim. Cosmochim. Acta* **56**, 2503–2520.
- Jacobsen B., Yin Q.-Z., Moynier F., Amelin Y., Krot A. N., Nagashima K., Hutcheon I. D. and Palme H. (2008a)  $^{26}\text{Al}$ – $^{26}\text{Mg}$  and  $^{207}\text{Pb}$ – $^{206}\text{Pb}$  systematics of Allende CAIs: canonical solar initial  $^{26}\text{Al}/^{27}\text{Al}$  ratio reinstated. *Earth Planet. Sci. Lett.* **272**, 253–364, doi:10.1016/j.epsl.2008.05.003.
- Jacobsen S. B., Chakrabarti R., Ranen M. C. and Petaev M. I. (2008b) High resolution  $^{26}\text{Al}$ – $^{26}\text{Mg}$  chronometry of CAIs from the Allende meteorite. *Lunar Planet. Sci.* **XXXIX**, #1999.
- Jungck M. H. A., Shimamura T. and Lugmair G. A. (1984) Ca isotopic variations in Allende. *Geochim. Cosmochim. Acta* **48**, 2651–2658.
- Krot A. N., Nagashima K., Hutcheon I. D., Davis A. M., Thrane K., Bizzarro M., Huss G. R., Papanastassiou D. A. and Wasserburg G. J. (2008) Oxygen isotopic compositions of individual minerals from FUN CAIs. *Lunar Planet. Sci.* **XXXIX**, #2162.
- Lee T., Papanastassiou D. A. and Wasserburg G. J. (1977)  $^{26}\text{Al}$  in the early solar system: fossil or fuel? *Astrophys. J.* **211**, L107–L110.
- Lee T., Papanastassiou D. A. and Wasserburg G. J. (1978) Ca isotopic anomalies in the Allende meteorite. *Astrophys. J.* **220**, L21–L25.
- Lee T., Russell W. A. and Wasserburg G. J. (1979) Calcium isotopic anomalies and the lack of aluminum-26 in an unusual Allende inclusion. *Astrophys. J.* **228**, L93–L98.
- Lee T., Chen W. H. and Chen J. C. (2011) Ca-43 isotopic anomaly in CAI and the astrophysical origin of Ca isotopes. *Lunar Planet. Sci.*, 42 #1828.
- MacPherson G. J. (2004) Calcium–aluminum-rich inclusions in chondritic meteorites. In *Treatise on Geochemistry*, No. 1 (ed. A. M. Davis). Elsevier, pp. 201–246.
- MacPherson G. J. and Davis A. M. (1994) Refractory inclusions in the prototypical CM chondrites, Mighei. *Geochim. Cosmochim. Acta* **58**, 5599–5625.
- MacPherson G. J., Wark D. A. and Armstrong J. T. (1988) Primitive materials surviving in chondrites: refractory inclusions. In *Meteorites and the Early Solar System* (eds. J. F. Kerridge and M. S. Matthews). University of Arizona Press, Tucson, pp. 746–807.
- MacPherson G. J., Nagashima K., Bullock E. S. and Krot A. N. (2008) Mass-dependent oxygen isotopic fractionation in non-FUN forsterite-bearing type B CAIs. *Lunar Planet. Sci.* **XXXIX**, #2039.
- Mason B. and Martin P. M. (1977) Geochemical differences among components of the Allende meteorites. *Smithson. Contrib. Earth Sci.* **19**, 84–95.
- Mason B. and Taylor S. R. (1982) Inclusions in the Allende meteorite. *Smithson. Contrib. Earth Sci.* **25**, 1–39.
- McCulloch M. T. and Wasserburg G. J. (1978a) Barium and neodymium isotopic anomalies in the Allende meteorite. *Astrophys. J.* **220**, L15–L19.
- McCulloch M. T. and Wasserburg G. J. (1978b) More anomalies from the Allende meteorite: samarium. *Geophys. Res. Lett.* **5**, 599–602.
- Moynier F., Simon J. I., Podosek F. A., Meyer B. S., Brannon J. and DePaolo D. J. (2010) Ca isotope effects in Orgueil leachates and the implications for the carrier phases of  $^{54}\text{Cr}$  anomalies. *Astrophys. J.* **718**, L7–L13, doi:10.1088/2041-8205/718/1/L7.
- Niederer F. R. and Papanastassiou D. A. (1984) Ca isotopes in refractory inclusions. *Geochim. Cosmochim. Acta* **48**, 1279–1293.
- Niederer F. R., Papanastassiou D. A. and Wasserburg G. J. (1985) Absolute isotopic abundances of Ti in meteorites. *Geochim. Cosmochim. Acta* **49**, 835–851.
- Papanastassiou D. A. (1986) Chromium isotopic anomalies in the Allende meteorite. *Astrophys. J.* **308**, L27–L30.
- Petaev M. I. and Jacobsen S. B. (2009) Petrologic study of AJ101, a new forsterite-bearing CAI from the Allende CV3 chondrite. *Geochim. Cosmochim. Acta* **73**, 5100–5114, doi:10.1016/j.gca.2008.10.045.
- Richter F. M. (2004) Timescales determining the degree of kinetic isotope fractionation by evaporation and condensation. *Geochim. Cosmochim. Acta* **68**, 4971–4992.
- Richter F. M., Davis A. M., Ebel D. S. and Hashimoto A. (2002) Elemental and isotopic fractionation of Type B calcium-, aluminum-rich inclusions: experiments, theoretical considerations, and constraints on their thermal evolution. *Geochim. Cosmochim. Acta* **66**, 521–540.
- Russell W. A., Papanastassiou D. A. and Tombrello T. A. (1978) Ca isotope fractionation on the Earth and other solar system materials. *Geochim. Cosmochim. Acta* **42**, 1075–1090.
- Simon J. I. and DePaolo D. J. (2010) Stable calcium isotopic composition of meteorites and rocky planets. *Earth Planet. Sci. Lett.* **289**, 457–466.



- Simon S. B., Davis A. M. and Grossman L. (1996) A unique ultrarefractory inclusion from the Murchison meteorite. *Meteorit. Planet. Sci.* **31**(1), 106–115.
- Simon S. B., Davis A. M., Grossman L. and McKeegan K. D. (2002) A hibonite-corundum inclusion from Murchison: a first-generation condensate from the solar nebula. *Meteorit. Planet. Sci.* **37**(4), 533–548.
- Simon J. I., DePaolo D. J. and Moynier F. (2009) Calcium isotope composition of meteorites, Earth and Mars. *Astrophys. J.* **702**, 707–715.
- Srinivasan G., Sahijpal S., Ulyanov A. A. and Goswami J. N. (1996) Ion microprobe studies of Efremovka CAIs: II. potassium isotope composition and  $^{41}\text{Ca}$  in the early solar system. *Geochim. Cosmochim. Acta* **60**, 1823–1835.
- Tanaka T. and Masuda A. (1973) Rare-earth elements in matrix, inclusions, and chondrules of the Allende meteorite. *Icarus* **19**, 523–530.
- Yin Q.-Z., Jacobsen S. B. and Yamashita K. (2002) Diverse supernova sources of pre-solar material inferred from molybdenum isotopes in meteorites. *Nature* **415**, 881–883.

Associate editor: Dimitri A. Papanastassiou